

Multimodal optical imaging of microvessel network convective oxygen transport dynamics

Casey deDeugd, Mamta Wankhede, and Brian S. Sorg*

J. Crayton Pruitt Family Department of Biomedical Engineering, University of Florida, Gainesville, Florida 32611, USA

*Corresponding author: brian.sorg@bme.ufl.edu

Received 2 September 2008; revised 17 December 2008; accepted 26 January 2009;
posted 27 January 2009 (Doc. ID 100736); published 2 March 2009

Convective oxygen transport by microvessels depends on several parameters, including red blood cell flux and oxygen saturation. We demonstrate the use of intravital microscopy techniques to measure hemoglobin saturations, red blood cell fluxes and velocities, and microvessel cross-sectional areas in regions of microvascular networks containing multiple vessels. With these methods, data can be obtained at high spatial and temporal resolution and correlations between oxygen transport and hemodynamic parameters can be assessed. *In vivo* data are presented for a mouse mammary adenocarcinoma grown in a dorsal skinfold window chamber model. © 2009 Optical Society of America

OCIS codes: 180.0180, 170.2655, 170.3880.

1. Introduction

Oxygen is required by mammalian cells for normal aerobic metabolism to produce energy for a cellular function [1]. Capillaries are not the only site of oxygen exchange [2], as significant exchange also occurs in precapillary arterioles [3] and postcapillary venules [4]. The complexity of microvascular oxygen transport and exchange with tissue is such that to this day the process is not completely understood [5,6]. There are a number of areas where a better understanding of microvascular oxygen transport may lead to advances. For example, abnormal microcirculatory function and oxygen transport is associated with several pathological conditions, including diabetes [7,8], hypertension [9,10], hemorrhagic shock [11,12], wound healing [13,14], and solid tumors [15–17]. Studies of normal physiologic function, such as functional activation of specific brain regions [18], can also benefit from further knowledge of microvascular oxygen transport function. Experimental studies, theoretical models, and their combination will play a role in these research areas.

Convective oxygen transport by the microcirculation can be mathematically described as a combination of parameters including red blood cell (RBC) oxygen carrying capacity and saturation, and blood flow measurements [6,19]. Hemoglobin saturation, hematocrit, and blood flow rate can be related to convective oxygen transport in a blood vessel per the following equation by Secomb *et al.* [19]:

$$Q_{\text{ox}}(P_{\text{O}_2}) = Q_{\text{bl}}[HC_{0,\text{RBC}}S_{\text{Hb}}(P_{\text{O}_2}) + \alpha_{\text{eff}}P_{\text{O}_2}], \quad (1)$$

where $Q_{\text{ox}}(P_{\text{O}_2})$ is the rate of oxygen transfer ($\text{cm}^3\text{O}_2/\text{s}$) and is a function of the blood partial pressure of oxygen (P_{O_2} , mmHg); Q_{bl} is the blood flow rate (cm^3/s); H is the hematocrit (dimensionless); $C_{0,\text{RBC}}$ is the oxygen carrying capacity of a RBC, which is the amount of oxygen bound in a fully saturated RBC ($\text{cm}^3\text{O}_2/\text{cm}^3$); S_{Hb} is fractional hemoglobin saturation (dimensionless), which is a function of blood P_{O_2} , and α_{eff} is the effective solubility of oxygen in blood ($\text{cm}^3\text{O}_2\text{cm}^{-3}\text{mmHg}^{-1}$), which is generally taken as a constant. This equation includes the amount of dissolved oxygen in the plasma, which is usually only a very small component of the amount of oxygen transported by the microcirculation relative to the amount transported by RBCs at atmospheric pressures. The microvascular hematocrit

term in Eq. (1) can be obtained from the following relation [20,21]:

$$H = \frac{V_{\text{RBC}} F_{\text{RBC}}}{\pi R^2 v_{\text{avg}}}, \quad (2)$$

where V_{RBC} is the average volume of RBCs (cubic centimeters), F_{RBC} is the RBC flux (number of RBCs per second), R is the radius of the blood vessel (centimeters), and v_{avg} is the average blood flow velocity (centimeters per second). A similar equation that describes microvascular convective oxygen transport given by Pittman [6] that does not include dissolved oxygen in the plasma is the following:

$$Q_{\text{ox}}(P_{\text{O}_2}) = \pi R^2 v_{\text{avg}} [\text{Hb}] S_{\text{Hb}}(P_{\text{O}_2}) C_{0,\text{Hb}}, \quad (3)$$

where $[\text{Hb}]$ is the concentration of hemoglobin (V/V , cm^3/cm^3), and $C_{0,\text{Hb}}$ is the amount of oxygen bound in a fully saturated unit volume of hemoglobin ($\text{cm}^3 \text{O}_2/\text{cm}^3$). Note that, despite their having the same units, there is a subtle yet important distinction between $C_{0,\text{Hb}}$ in Eq. (3) and $C_{0,\text{RBC}}$ in Eq. (1): $C_{0,\text{RBC}}$ refers to a single RBC and is normalized to the volume of the RBC, while $C_{0,\text{Hb}}$ refers to hemoglobin volume in the context of hemoglobin concentration. If the dissolved oxygen term in Eq. (1) is neglected, then effectively Eqs. (1) and (3) are equivalent in that they both describe the volume of oxygen being transported in the blood vessel per unit time in terms of the volume of hemoglobin being transported per unit time and the amount of oxygen being carried by the hemoglobin.

A number of optical techniques capable of microvascular oxygenation measurement have been developed, including spectroscopic methods [22–27] and phosphorescence quenching techniques [23,28–31]; however, measurement of microvascular convective oxygen transport requires knowledge of additional hemodynamic and functional parameters besides oxygenation. Researchers have employed intravital microscopy imaging techniques to determine convective oxygen transport in microvessel segments and branches. In a notable example, Swain and Pittman measured convective oxygen transport in individual microvessel branches in hamster cheek pouch retractor muscles to identify longitudinal gradients of oxygen in precapillary arterioles, thus demonstrating diffusion of oxygen out of these vessels into the surrounding tissue [32]. In this paper, we endeavored to identify a particular combination of intravital microscopy optical techniques to simultaneously capture the relevant parameters necessary to measure convective oxygen transport from a microvascular network region such that high spatial and temporal resolution and correlations of oxygen transport could be achieved across the network. Three different optical techniques were employed: wide-field spectroscopic measurements for microvessel hemoglobin saturation, wide-field fluorescence measurements for RBC flux and velocity, and confocal fluorescence

measurements for a microvessel cross-sectional area. The measured parameters were used with the previously described equations to calculate the convective oxygen transport throughout a microvessel network. The abnormal oxygen transport in tumors provided the motivation for this research; thus the *in vivo* model chosen was tumors grown in mouse dorsal skinfold window chambers. Furthermore, the advantages and limitations of the method presented in this study are discussed.

2. Materials and Methods

A. Tumor Cells

4T07 mouse mammary adenocarcinoma cells, a nonmetastatic subclone of the 4T1 cell line, were cultured as a monolayer in DMEM (Dulbecco's Modified Eagles's Medium, Mediatech, Manassas, Virginia) with 10% fetal bovine serum (Mediatech, Manassas, Virginia). The tumor cells were a gift from Mark W. Dewhirst (Duke University, Durham, North Carolina). Cultures were used after one or two passages from frozen stocks to ensure recovery from the thermal shock and a normal growth rate. The cells were enzymatically dissociated from the flasks (BD Bioscience, San Jose, California) by using 0.05% trypsin/EDTA (ethylenediaminetetraacetic acid, Mediatech, Manassas, Virginia) to prepare single-cell suspensions. Cells were counted via a hemacytometer to determine the cell concentration.

B. Preparation of Fluorescent Red Blood Cells

RBCs were fluorescently labeled by using a modification of the procedure by Unthank *et al.* [33]. RBCs obtained from donor mice were labeled with a 1 mg/ml stock solution of Carbocyanine dye 1,1'-dioctadecyl-3,3,3',3'-tetramethylindodicarbocyanine, 4-chlorobenzenesulfonate salt (DiD solid, Invitrogen, D-7757) dissolved in ethanol. DiD (excitation 644 nm/emission 665 nm) was chosen as the lipid membrane labeling solution because it is an analog of the commonly used DiI dye (ex 549 nm/em 565 nm), but with a markedly redshifted fluorescence excitation and emission spectrum to minimize interference of RBC flux measurements with hemoglobin saturation measurements (500–575 nm). RBCs obtained by cardiac puncture from a donor mouse were washed twice via centrifugation and resuspension in phosphate buffered saline (PBS). The cells were labeled by adding 100 μl of cells and 100 μl of DiD stock solution to 10 ml of sterile PBS. The solution was incubated at room temperature for 30 min and agitated every 10 min to ensure suspension of the RBCs. After labeling, the RBCs were washed to remove unbound dye and resuspended in PBS. Immediately prior to an imaging session, a 50 μl bolus of packed labeled cells in saline solution (30% V/V) was administered to the mouse to be imaged by tail vein injection. An aliquot of DiD labeled cells was saved for flow cytometric confirmation of the efficacy of the labeling procedure.

C. Animal Model and Imaging

All *in vivo* procedures were conducted in accordance with a protocol approved by the University of Florida Institutional Animal Care and Use Committee. A total of seven athymic (nu/nu) female nude mice weighing at least 21 g (Charles River Laboratories, Raleigh, North Carolina) were surgically implanted with a titanium window chamber under anesthesia (ketamine 100 mg/kg IP and xylazine 10 mg/kg IP) on the dorsal skin flap. Tumors were established at the time of window chamber surgery from a 10 μ L single-cell suspension of 5×10^3 to 10×10^3 4TO7 cells injected into the subcutaneous tissue immediately prior to placing a 12 mm round glass coverslip over the exposed area of the skin. Animals were housed postsurgery in an environmental chamber maintained at 33°C and 50% humidity with free access to food and water and standard 12 h light–dark cycles. Experiments were conducted after the tumor had been well established, with three of the five animals being imaged twice. Tumors suitable for our experiments were typically obtained 8–13 days after implantation.

For spectral and RBC flux imaging, mice were placed on the microscope stage on a heating pad to maintain normal body temperature and were anesthetized by 1%–2% isoflurane in air. In two experiments, an increase in convective oxygen transport was induced during imaging by a change in breathing gases from room air to 100% oxygen.

D. Spectral Imaging

The spectral imaging system, image acquisition, and image processing methods for hemoglobin saturation measurements were discussed in detail previously [26]. Briefly, one hemoglobin saturation image set comprised 16 images acquired in the wavelength range of 500–575 nm with an interval of 5 nm. Automated spectral image acquisition was performed by using customized LabVIEW software (National Instruments, Austin, Texas). A Zeiss microscope (Carl Zeiss, Inc., Thornwood, New York) was used as the imaging platform. For transillumination of window chambers, a 100 W tungsten halogen lamp was used. Images were obtained at 1380×1035 pixels and 12 bit dynamic range by using a CCD camera thermoelectrically cooled to -20°C (DVC Company, Austin Texas, Model 1412AM-T2-FW). The long-working-distance objectives used were 2.5 \times and 5 \times Fluars, 10 \times EC Plan-NeoFluar, and a 20 \times LD-Plan-NeoFluar (Carl Zeiss, Inc., Thornwood, New York). A liquid crystal tunable filter (CRI, Cambridge, Massachusetts) with a 400–720 nm transmission range and a 10 nm nominal bandwidth placed in front of the camera provided band-limited images. Images were saved as 16 bit TIFF files. For image processing, all 16 images per set were converted to double-precision arrays in MATLAB (The Mathworks Inc., Natick, Massachusetts). Using the linear least squares method proposed by Shonat *et al.* [23], we converted images on a pixelwise basis to relative values of

hemoglobin saturation. Hemoglobin saturation pseudocolor maps of the microvessel networks were created from the spectral image data by a linear least squares regression fit of a model of the microvessel absorbance to the data using pure oxyhemoglobin and deoxyhemoglobin reference spectra. Regions of interest for hemoglobin saturation measurements were selected on the basis of the proximity of the microvessel region to areas selected for RBC flux measurements. Customized LabVIEW software enabled automated image acquisition using the specifications for camera exposure time and gain for each filter wavelength. Given that the liquid crystal tunable filter transmits less at shorter wavelengths and more at longer wavelengths, the exposure time for the camera was controlled such that the full dynamic range of the camera was utilized. The minimum exposure time used was 400 ms for the longest wavelength, whereas the maximum exposure time used was 1400 ms for the shortest wavelength, resulting in a typical acquisition time of approximately 16 s for image acquisition, filter tuning, image transfer, and saving images on an external hard drive.

E. RBC Flux Imaging

Fluorescently labeled RBCs were imaged via streaming video using an Andor iXon electron multiplying CCD camera (Andor Technology, South Windsor, Connecticut). A Cy5 filter set was used (Chroma Technology Corp., Rockingham, Vermont, excitation 640 nm with 20 nm bandwidth, emission 680 nm with 30 nm bandwidth) in line with the illumination source of a Zeiss FluoArc mercury lamp. To optimize the resolution of the fast-moving cells, data were acquired in kinetic acquisition mode with 2×2 binning, using an exposure time of 16.2 ms, a shift speed of 0.564 μ s, and a frequency of ~ 30 Hz to ensure that images would be captured with sufficient temporal resolution. Internal triggering was used to spool data directly to the computer hard drive, and 20 s of streaming video was saved every minute for 1 h in coordination with the acquisition of spectral imaging data sets. Each frame was saved as a tagged image format file (TIFF), resulting in a stack of 600 TIFFs per data point. RBC flux was determined by first identifying a region on a vessel of interest where flowing RBCs appeared to be in good focus and then manually counting the number of labeled cells flowing past the designated location on the vessel over the 20 s time interval of data acquisition for the time point. These measurements were converted to flux by correcting for the fraction of labeled RBCs versus unlabeled RBCs in the mouse blood. The fraction of labeled RBCs was determined by flow cytometry of a blood sample obtained postimaging via retro-orbital puncture performed on the imaged mouse. The RBC flux was then calculated by using Eq. (4):

$$F_{\text{RBC}} = \frac{N_{\text{RBC}}}{t \left(\frac{N_{\text{RBC,fluor}}}{N_{\text{RBC,total}}} \right)}, \quad (4)$$

where N_{RBC} is the number of fluorescent RBCs counted flowing in the vessel, t is the time interval in which N_{RBC} was counted (20 s in this case), and $N_{\text{RBC,fluor}}$ and $N_{\text{RBC,total}}$ are the number of fluorescent and total RBCs, respectively, counted by flow cytometry in the postexperiment blood sample.

RBC velocity was determined from the time required for an individual RBC to travel a specific distance in the blood vessel that passed through the region of interest. The time interval was determined from the frame rate of fluorescence video imaging. The mean velocity of 5–10 randomly selected RBCs from each time point was taken as v_{avg} .

F. Laser Scanning Microscopy

After hyperspectral imaging sessions, animals were moved to an Olympus IV100 laser scanning microscope (LSM). Before imaging, mice were anesthetized using injectable anesthesia (ketamine 100 mg/kg IP and xylazine 10 mg/kg IP), and placed on a heating pad. A 4 mg/ml stock solution of β -phycoerythrin (P-800, Invitrogen, Carlsbad, California) was diluted to approximately 18.7% V/V in sterile saline in order to obtain a weight of 0.075 mg per 100 μl bolus, which is the weight/volume used in a protocol obtained from Brizel *et al.* [20], and 50–100 μl of this solution was delivered via tail vein injection. β -phycoerythrin was chosen to illuminate the blood vessels because it is a plasma binding dye that has a very broad and bright emission spectrum (ex 542 nm, em 550–700 nm, with peak $\lambda = 575$ nm). This was suitable for the laser source that was available for the LSM, which has a solid-state laser tuned to 561 nm that was used for excitation. This wavelength closely coincides with a secondary excitation peak of β -phycoerythrin. Images of areas that had been analyzed via hyperspectral imaging and RBC flux were used as a reference to locate the same regions with the LSM. Once the regions were located visually, 3D automated scanning was performed by acquiring $x-y$ images of the 10 \times objective area and stepping through the z direction in 5–10 μm step sizes. While a maximal image depth of about 300 μm could reasonably be expected with the LSM system, imaging was performed only to a depth of 50–100 μm which included the top tumor vessel layer in the window chamber. The main reason for the limitation in image depth was that data acquisition at high axial spatial resolution increased imaging time, which increased the probability that a motion artifact that could ruin the data set might occur during imaging. Despite the fact that the window chamber was firmly secured to the imaging platform, the skin could still move within the window chamber owing to a reflexive muscle twitch or a deep breath by the animal. Additional restraints on animal and skin movement during imaging could possibly enable imaging to a greater depth.

Data obtained via LSM were originally saved to the proprietary Olympus software as 16 bit TIFF files that were subsequently converted to 8 bit by using ImageJ software. The 8 bit images were then

loaded into Image Surfer, a 3D image reconstruction freeware program for visualization and analysis of 3D images and data sets [34]. The software uses deconvolution techniques to provide volume rendering of image stacks and allows user manipulation of the volume in the x , y , and z dimensions.

3. Results

Absorption from the fluorescent dye used to label the RBCs could potentially affect the calculation of hemoglobin saturation if the fraction of labeled cells is high enough. In this case, the dye absorption would have to be accounted for in the calculation. As shown in Fig. 1, the effect of absorption from the RBC fluorescent labeling dye on calculations of hemoglobin saturation was determined for various fractions of labeled RBCs with 100% oxygen saturation flowing in glass capillary tubes. To observe the effect, dye absorption was not accounted for in the hemoglobin saturation calculation. It can be seen in Fig. 1 that, at RBC labeling fractions less than 5%, the effect of dye absorption is negligible, while larger labeled fractions cause progressively more interference. In this study, the fraction of labeled RBCs in the mice was in the range of 1%–3% as determined by flow cytometry of blood samples taken from the mice at the end of each experiment; so the labeled RBCs had a negligible effect on the hemoglobin saturation calculation.

Figures 2–9 illustrate how the multimodality image data (Figs. 2–6) were used to obtain microvessel functional and hemodynamic data (hemoglobin saturation and RBC flux in Figs. 7 and 8) for the calculation of microvessel convective oxygen transport (Fig. 9). A transmitted light image of an example tumor microvessel network is shown in Fig. 2, and a corresponding hemoglobin saturation map for the

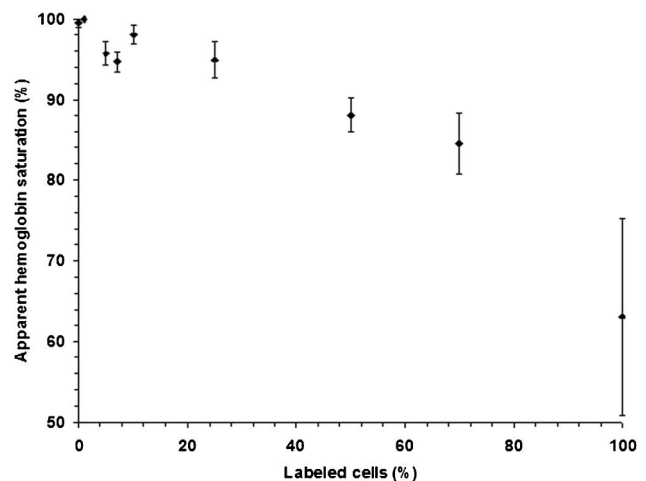


Fig. 1. Plot of apparent hemoglobin saturation of different fractions of RBCs labeled with DiD. The absorption of the fluorescent dye is not taken into account in the hemoglobin saturation calculation in order to observe the effect of the fluorescent dye absorption. The data points are the mean \pm standard deviation of a region of pixels in an image of RBCs with 100% hemoglobin saturation in a glass capillary tube. The standard deviation for the two lowest labeled fractions of RBCs is less than 1%.

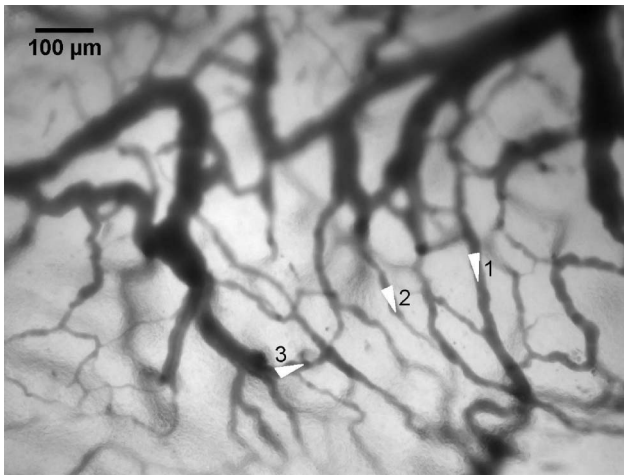


Fig. 2. Transmitted light image of the tumor microvessel network. White triangles represent regions of interest chosen for analysis. A 10× objective was used for imaging (NA of 0.3, working distance of 5.5 mm).

network is shown in Fig. 3. In Fig. 4 is an image of flowing fluorescently labeled RBCs flowing in the microvessel network. Data regarding dynamic changes in hemoglobin saturation, RBC flux, and blood flow were derived from data sets with the images in Figs. 3 and 4. Confocal image data (Fig. 5) were acquired on an Olympus IV100 system after 1 h of imaging of hemoglobin saturation and RBC flux. A 10× objective was used for imaging in both microscope systems. Since data for Figs. 3–5 were acquired in two different imaging systems, relocation of the animal was required, but it was still possible to locate the original imaged region. The confocal data were used to measure the cross-sectional area of the microvessel regions of interest for analysis. In Fig. 6 is a 3D reconstructed confocal image stack of the area imaged in Figs. 2–5 showing a cross-sectional area across the dashed line in Fig. 5. The cross-sectional areas marked in the figure are for the regions of interest marked 1 ($481 \mu\text{m}^2$) and 2 ($324 \mu\text{m}^2$) in Fig. 2.

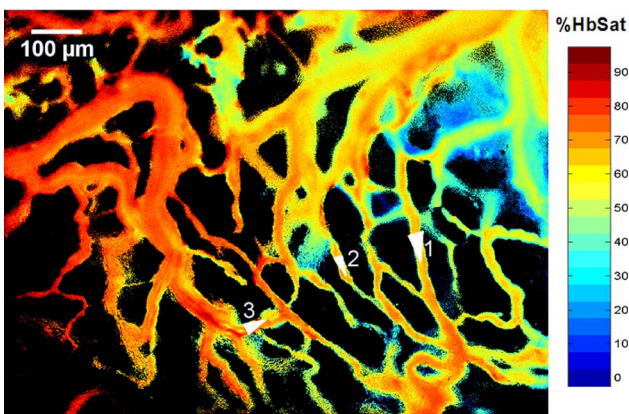


Fig. 3. (Color online) Hemoglobin saturation image of the tumor microvessel network in Fig. 2. The pixels are colored according to the hemoglobin saturation scale to the right of the figure. The background is black. Regions of interest for analysis are indicated in the figure.

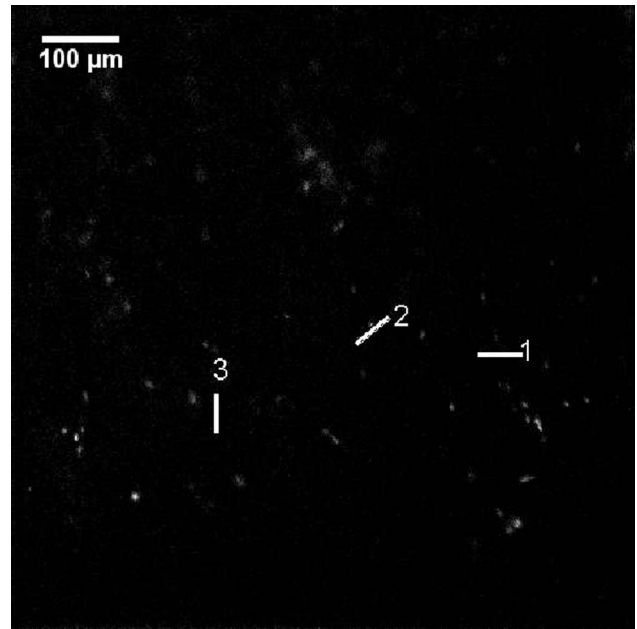


Fig. 4. Fluorescence image of RBCs labeled with DiD flowing in the tumor microvessel network. Images were captured with an electron multiplying CCD camera at video rates ($\sim 30 \text{ Hz}$). 20 s of data were taken every minute of the hour-long imaging session, and cells were counted over this time increment and then converted to RBC flux measurements. The locations of the regions of interest for analysis are indicated in the figure.

Figures 7 and 8 show example plots of RBC flux and hemoglobin saturation over time for regions of interest 1 and 3 from Fig. 2. It can be seen from the figures that trends in the hemoglobin saturation dynamic

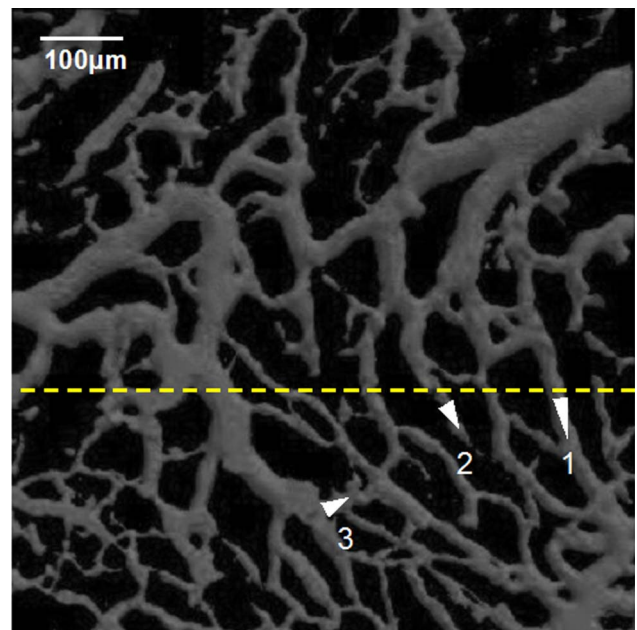


Fig. 5. (Color online) Confocal z-stack projection of the tumor microvessel network in Fig. 2. A total of 49 images were acquired at $5 \mu\text{m}$ intervals to a total depth of $245 \mu\text{m}$ by using an Olympus IV100 LSM. Regions of interest for analysis are indicated. The dashed line indicates the location of the cross-sectional area in Fig. 6.

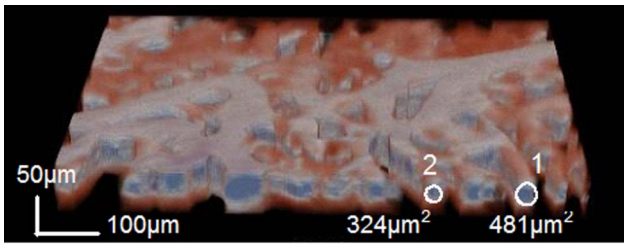


Fig. 6. (Color online) Microvessel cross-sectional areas were measured from confocal image stack data. The cross-sectional area was calculated using the number of pixels in the vessel cross section and the dimensions of a pixel in the image plane. The dashed line in Fig. 5 indicates the location of the cross-sectional area.

changes in general are similar to trends in RBC flux fluctuations. An example of the oxygen transport parameters that can be measured with this technique is demonstrated with the vessels marked with region of interest numbers 1 and 2 in Fig. 2. The time-averaged RBC velocity for vessels 1 and 2, respectively, is 442 and $98 \mu\text{m/s}$. Using an approximate RBC volume of $40 \mu\text{m}^3$ derived from mouse hematological data [35] with measured RBC flux, vessel cross-sectional area, and RBC velocity data in Eq. (2), the time averaged hematocrits for vessels 1 and 2 are 0.14 and 0.08 , respectively. Taking the maximal oxygen carrying capacity of RBC [$C_{0,\text{RBC}}$ in Eq. (1)] as $0.5 \text{ cm}^3 \text{ O}_2/\text{cm}^3$ [32], then the measured data were used with the previously defined equations to obtain the convective oxygen transport over time in the two vessels as plotted in Fig. 9. Fourier analysis was performed on the time series data in Fig. 9, and the mean-subtracted normalized power spectra of the convective oxygen transport data are shown in Fig. 10. The dominant fluctuation frequency is less than 0.2 cycles/min , which is consistent with previously measured 4T1 tumor hemoglobin saturation fluctuation data obtained with our imaging system [25] and reported pO_2 fluctua-

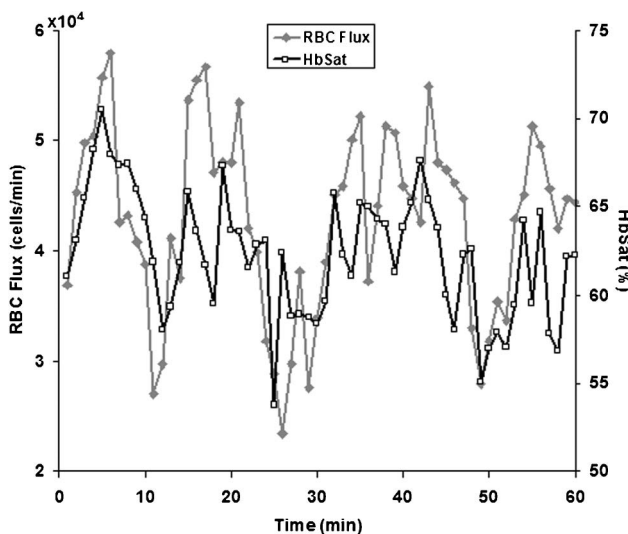


Fig. 7. Plot of RBC flux versus hemoglobin saturation (HbSat) for region of interest 1 in Fig. 2. The data points were acquired at 1 min intervals for 1 h.

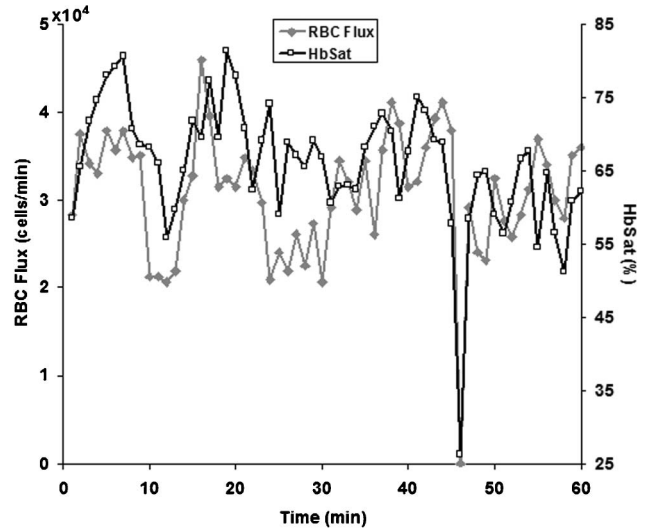


Fig. 8. Plot of RBC flux versus hemoglobin saturation (HbSat) for region of interest 3 in Fig. 2. The data points were acquired at 1 min intervals for 1 h.

tions in a variety of tumor types measured with oxygen microelectrodes ([36–40]).

Perturbations to convective oxygen transport can be measured with this technique. For the tumor network shown in Fig. 11, the mouse initially was breathing normal air during the imaging session and after 20 min was switched to 100% oxygen breathing. The tumor microvessel network with indicated regions of interest and a graph of convective oxygen transport over time are shown, respectively, in Figs. 11 and 12. An increase in the average convective oxygen transport with 100% oxygen

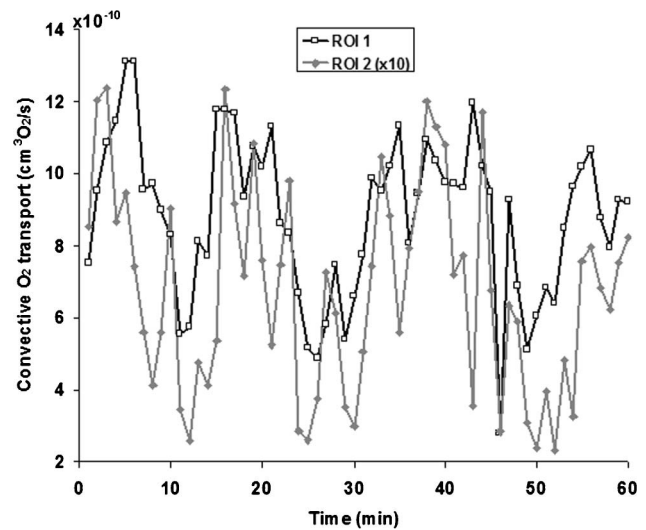


Fig. 9. Convective oxygen transport over time for regions of interest 1 and 2 in Fig. 2. Note that the values for region of interest 2 are plotted as $10\times$ their actual value for clarity. The oxygen transport in these vessels tends to fluctuate together, although vessel 1 is transporting about $10\times$ more oxygen than vessel 2. It should be noted that there was difficulty in imaging RBCs at the 6 min time point for vessel 2; so the RBC flux was interpolated for that data point.

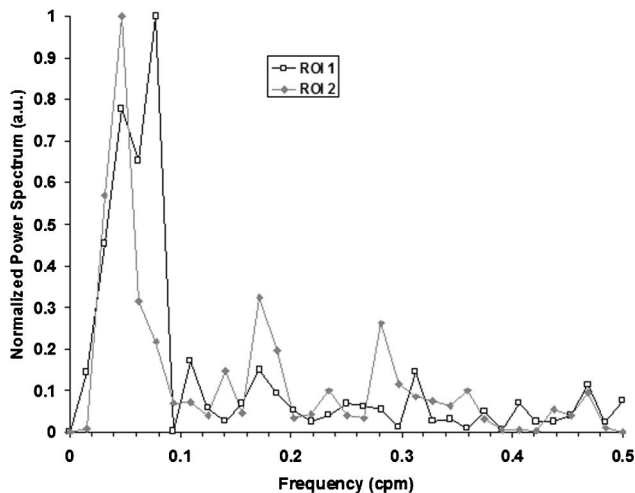


Fig. 10. Normalized power spectra for the convective oxygen transport time series data in Fig. 9 obtained by Fourier analysis. The frequency scale is given in cycles per minute (cpm).

breathing was measured (see Table 1). Unlike ROI 1, the increase in average convective oxygen transport in ROI 2 was not statistically significant. This may be a result of the increase in magnitude of the fluctuations that occurred in ROI 2 after oxygen breathing (air breathing standard deviation $1.0 \text{ cm}^3 \text{ O}_2/\text{s}$, 100% breathing standard deviation $1.8 \text{ cm}^3 \text{ O}_2/\text{s}$). An increase in the magnitude of tumor $p\text{O}_2$ fluctuations with 100% oxygen breathing has been previously reported [37]. By way of comparison, the data in Fig. 9 for regions of interest 1 and 2 in Figs. 2–6 were divided into time periods of 1–30 and 31–60 min, and the average convective oxygen transport for each time was period calculated. As is shown in Table 1, there was virtually no change in the average convective oxygen transport in the two time periods when the mouse breathed room air alone for the duration of the experiment.

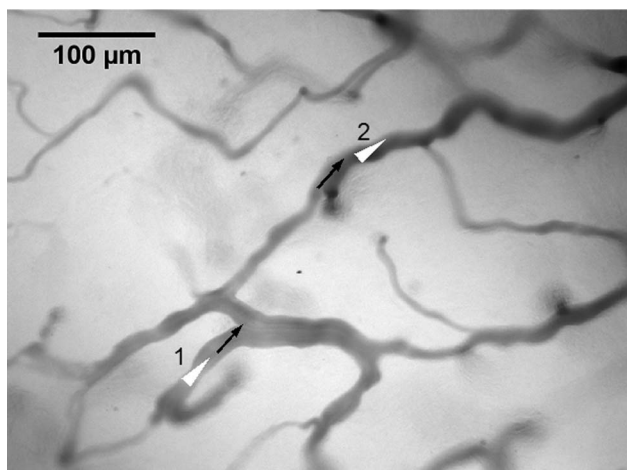


Fig. 11. Transmitted light image of the tumor microvessel network for Fig. 12. White triangles represent regions of interest chosen for analysis. Arrows indicate blood flow direction in the vessels around the regions of interest. A $10\times$ objective was used for imaging (NA of 0.3, working distance of 5.5 mm).

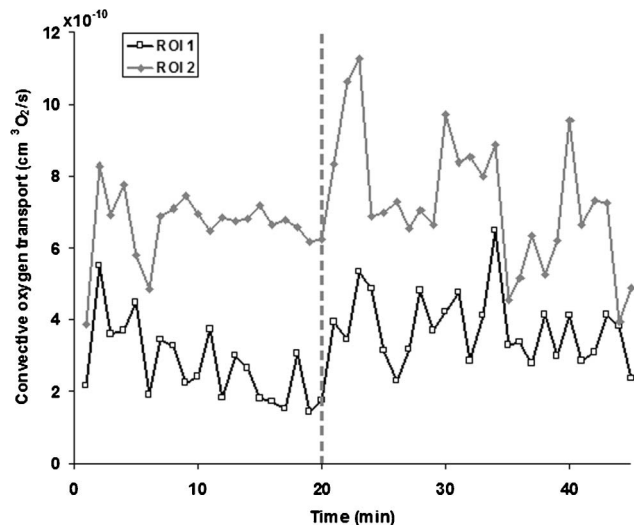


Fig. 12. Convective oxygen transport over time for regions of interest 1 and 2 in Fig. 11. The mouse initially started breathing normal air and was switched to 100% oxygen breathing during the experiment. The vertical dashed line indicates the point at which 100% oxygen breathing was started.

4. Discussion

Convective oxygen transport in individual microvessel branches has been measured using optical techniques. Swain and Pittman used microspectrophotometry to measure hemoglobin saturation and hemoglobin concentration, a dual detector cross-correlation technique to measure blood velocity, and video measurements of vessel diameter to calculate the vessel cross-sectional area [32]. Using these measurements, the authors were able to calculate convective oxygen transport in segments of hamster cheek pouch retractor muscle microvessels. In this study, we sought to expand upon previous techniques by developing a method to enable high spatial and temporal resolution and correlations of convective oxygen transport to be achieved across an entire network region rather than interrogating blood vessel segments individually at different points in time. To achieve this goal, a spectral imaging technique developed previously [26] was employed to capture hemoglobin saturation information from the microvessel network. As a wide-field imaging modality, this technique enables temporal and spatial correlation of fluctuations of hemoglobin saturation across the network [25]. Wide-field fluorescence imaging was chosen for the same reason to obtain RBC flux and velocity information across the microvessel network. Confocal imaging was used to obtain accurate microvessel cross-sectional areas rather than assuming a circular vessel cross section. Confocal imaging also enables more comprehensive measurements of microvessel positions within the tissue and relative to other branches in the network. It should be noted that intraluminal variations in hemoglobin saturation and RBC flux or velocity are possible [41], and the technique described in this paper does not address this issue. Rather, the intent was to

Table 1. Comparison of Tumor Microvessel Convective Oxygen Transport in Sequential Time Periods with Air Breathing Alone or Air Breathing and 100% Oxygen Breathing

Microvessel		Average Convective Oxygen Transport ($\text{cm}^3 \text{O}_2/\text{s}$) (mean \pm SEM ^a)			
Fig.	ROI	Air, 1–30 min	Air, 1–20 min	Air, 31–60 min	100% O ₂ , 21–45 min
2	1	$8.8 \times 10^{-10} \pm 0.4 \times 10^{-10b}$		$8.9 \times 10^{-10} \pm 0.4 \times 10^{-10b}$	
2	2	$6.7 \times 10^{-11} \pm 0.6 \times 10^{-11b}$		$6.8 \times 10^{-11} \pm 0.5 \times 10^{-11b}$	
11	1		$2.8 \times 10^{-10} \pm 0.2 \times 10^{-10c}$		$3.8 \times 10^{-10} \pm 0.2 \times 10^{-10c}$
11	2		$6.6 \times 10^{-10} \pm 0.2 \times 10^{-10b}$		$7.3 \times 10^{-10} \pm 0.4 \times 10^{-10b}$

^aStandard error of mean.

^bNot statistically different, *t* test.

^cStatistically significantly different, *t* test, *p* < 0.01.

make macroscopic observations across network regions; thus the measured parameters can be considered average or integrated values within the microvessels.

As can be seen from Fig. 1, the fraction of *in vivo* labeled RBCs in these experiments was such that absorption from the fluorescent dye did not have an effect on the calculation of hemoglobin saturation. If this were a concern, it would be relatively easy to account for the dye absorption by including it in the regression equation for calculation of hemoglobin saturation. It would be necessary to use a dye absorption spectrum that was acquired on the spectral imaging system for this purpose. Figures 2–12 demonstrate how multimodal optical imaging can be used to acquire imaging data on hemoglobin saturation, RBC flux, velocity, and hematocrit, and microvessel cross-sectional area that can be used to calculate convective microvascular oxygen transport in a local network region, in this case a tumor microvessel network. Fluctuations in hemoglobin saturation in the microvessels were similar to changes in RBC flux, as can be seen in Figs. 7 and 8. Spontaneous arteriolar vasomotion can cause fluctuations in blood flow and has been documented in a variety of normal tissues [42–44]. Acute fluctuations in tumor blood flow that contribute to tumor oxygen fluctuations have also been documented [36,38,45,46] and are believed to be caused by a combination of factors, including tumor feeding vessel vasomotion, dynamic changes in RBC rheology and flow resistance, and intussusceptive angiogenesis [36,47]. The correlation between RBC flux and hemoglobin saturation in Figs. 7 and 8 was expected, as previous measurements of RBC flux and perivascular oxygen tension made with microelectrodes have shown such a relationship in tumor microvessels [45]. The measured time-averaged RBC velocity, flux, and microhematocrit values in this study were comparable with those obtained for similarly sized microvessels in a rat mammary adenocarcinoma [20].

The main advantage of the technique described in this paper is the ability to perform simultaneous imaging and measurements of microvessel hemoglobin saturation and RBC flux across a microvessel network region. This can enable analysis of complex convective oxygen transport relationships among

vessels in a local network region. Our technique for measurement of oxygen delivery may potentially be combined with other techniques to measure oxygen deposition or utilization in tissue to give a more complete picture of tissue oxygen supply and demand. For example, the fluorescent hypoxia marker EF5 can highlight tissue areas that have been exposed to hypoxia [48], and this can be compared with the convective oxygen transport in the supply vessel networks. The fluorescent respiratory metabolites NADH (reduced nicotinamide adenine dinucleotide) and FAD (flavin adenine dinucleotide) may be used to compute redox ratios [49] to provide a relative measure of tissue oxidative metabolism in response to oxygen delivery. Phosphorescence lifetime imaging may be utilized to measure tissue oxygen tension [23,29] to form a more complete picture of oxygen delivery and deposition in tissue. The combination of additional techniques will increase the technical complexity of experimental procedures and may be subject to various limitations. There are several research areas where a complete picture of tissue oxygen supply and demand may be beneficial. These include studies of tumor angiogenesis, treatment with antiangiogenic agents, and measurement of changes in tumor microvessel function [50], investigations of vascular pathologies that contribute to cerebral ischemia and brain injury [51], and studies of impaired oxygen delivery and hypoxia in various retinopathies due to pathological angiogenesis [52].

A limitation of the technique is the shallow depth that can be imaged by using spectral imaging for the hemoglobin saturation measurements. This will restrict investigations to more superficial vessels in most tissues with the exception of a few specific cases, such as mesentery tissue, which is relatively transparent and 2D. Another constraint is that the RBC flux measurement technique places a limit on the distribution of vessel diameters that can be measured and the size of the field of view that can be used. It is difficult to accurately measure RBC flux in larger vessels because some of the deeper labeled RBCs in a large-diameter vessel may be shielded by shallower RBCs in the vessel and therefore may not be imaged. Also, larger vessels have larger microhematocrits, which makes it difficult to discriminate individual labeled RBCs. The field of view is limited to

a size such that single flowing labeled RBCs can be resolved and imaged reliably. If microvessel diameters changed during imaging owing to a change in vascular muscle tone, then the cross-sectional areas measured with confocal microscopy may not represent the actual value at the previously measured time points during spectral and fluorescence imaging. However, in tumors, microvessels are abnormal with little to no smooth muscle or innervation [53]; so this occurrence is less likely, but in normal tissues spontaneous vasomotion is common [42–44]. Errors in the microvessel cross-sectional area can affect calculations of microvessel hematocrit and convective oxygen transport. However, if Eq. (1) is used for calculation of convective oxygen transport with the plasma oxygen transport term neglected, then the effects of microvessel diameter changes can be avoided if the product of the microvessel cross-sectional area and average RBC velocity ($\pi R^2 V_{\text{avg}}$) is used to calculate volumetric blood flow (Q_{bl}) in Eq. (1), as is effectively done in Eq. (3), so the $\pi R^2 V_{\text{avg}}$ term will cancel the denominator in the hematocrit term H ; see Eq. (2).

Two-photon microscopy (TPM) has been used to measure microvascular oxygenation (pO_2) with phosphorescence lifetime imaging [54], blood velocity [55], and microvessel morphology [56]. TPM also has the potential to measure hemoglobin saturation [57]. An appropriate combination of these methods may enable measurement of convective oxygen transport in microvessel networks in 3D with greater imaging depth than the technique described in this paper. The scanning beam nature of TPM can limit the spatial and temporal correlations of dynamic changes in convective oxygen transport across the network, depending on the time scale of the dynamic events being measured and the image acquisition speed of the instrument. A more severe limitation is that TPM measurements of blood velocity require scanning of the imaging laser beam parallel to the axis of blood flow in each individual measured microvessel segment, which can be time consuming and impractical in the case of networks with complex geometries. Wide-field phosphorescence lifetime imaging has been combined with imaging of fluorescently labeled RBCs [58], thus enabling simultaneous acquisition of microvessel oxygenation and RBC velocity or flux across a network. A problem with phosphorescence lifetime imaging is that it can be difficult to use for measurements of microvascular convective oxygen transport. Recall from Section 1 that convective oxygen transport is a measurement of the amount of oxygen transported by blood flow, which predominantly occurs as oxygen bound to hemoglobin in RBCs and can be determined from measurements of hemoglobin saturation (percent of maximal hemoglobin oxygen carrying capacity) [6,19]. Phosphorescence lifetime imaging measures the amount of diffusing oxygen (pO_2) available to interact with a phosphorescent dye [6]. While hemoglobin saturation can be related to ambient pO_2 through the

hemoglobin–oxygen dissociation curve, the shape of the curve is dependent on the local pH and pCO_2 [1,5]; so unless these factors are somehow known, inaccurate calculations of hemoglobin saturation may be obtained. This is especially true in tumor microenvironments, which are known to have pathologically acidotic pH values [30,59]. Spectral imaging has been combined with laser speckle contrast imaging for simultaneous wide-field imaging of microvascular hemoglobin saturation and blood flow [22]. However, laser speckle contrast provides only relative measurements of perfusion [60]. Techniques for absolute velocity measurements with laser speckle and Doppler techniques are in development but currently not reliable enough for routine use with tissue [61]. Several recent papers provide evidence that optical coherence tomography (OCT) may have the potential to make 3D measurements of microvessel convective oxygen transport from endogenous signals with a single imaging modality. Doppler OCT can provide blood velocity information [62,63], and blood flow can be mapped in 3D microvessel networks [64]. Blood flow measurements with OCT can be made with flow rates measured in terms of absolute blood volumes [65]. Measurements of hemoglobin saturation in blood vessels using OCT are in development [66,67], and a recent *in vivo* study demonstrated that precise hematocrit measurement using OCT is feasible [68]. These techniques have not yet been combined to demonstrate convective oxygen transport measurements with OCT. The spatial resolution and relatively low hemoglobin absorption in the wavelength range typically used for OCT may restrict such measurements to vessels with larger diameters and hematocrits.

In summary, we have developed a multimodality optical imaging technique to measure microvascular convective oxygen transport with high spatial and temporal resolution across a microvessel network region. We demonstrated this technique *in vivo* in a mouse window chamber tumor model. This technique may be useful for investigations of complex oxygen transport dynamics in microvessel networks.

C. deDeugd and M. Wankhede contributed equally to this work.

References

1. A. C. Guyton, *Textbook of Medical Physiology* (W. B. Saunders, 1991).
2. B. R. Duling and R. M. Berne, "Longitudinal gradients in periarteriolar oxygen tension," *Circ. Res.* **27**, 669–678 (1970).
3. B. R. Duling, "Microvascular responses to alterations in oxygen tension," *Circ. Res.* **31**, 481–489 (1972).
4. R. D. Shonat and P. C. Johnson, "Oxygen tension gradients and heterogeneity in venous microcirculation: a phosphorescence quenching study," *Am. J. Physiol. Heart Circ. Physiol.* **272**, H2233–H2240 (1997).
5. A. G. Tsai, P. C. Johnson, and M. Intaglietta, "Oxygen gradients in the microcirculation," *Physiol. Rev.* **83**, 933–963 (2003).
6. R. N. Pittman, "Oxygen transport and exchange in the microcirculation," *Microcirculation* **12**, 59–70 (2005).

7. R. L. Greenman, S. Panasyuk, X. Wang, T. E. Lyons, T. Dinh, L. Longoria, J. M. Giurini, J. Freeman, L. Khaodhiar, and A. Veves, "Early changes in the skin microcirculation and muscle metabolism of the diabetic foot," *Lancet* **366**, 1711–1717 (2005).
8. P. E. James, D. Lang, T. Tufnell-Barret, A. B. Milsom, and M. P. Frenneaux, "Vasorelaxation by red blood cells and impairment in diabetes: reduced nitric oxide and oxygen delivery by glycated hemoglobin," *Circ. Res.* **94**, 976–983 (2004).
9. M. A. Boegehold, "Microvascular structure and function in salt-sensitive hypertension," *Microcirculation* **9**, 225–241 (2002).
10. J. J. Mourad and M. Laville, "Is hypertension a tissue perfusion disorder? Implications for renal and myocardial perfusion," *J. Hypertens.* **24**, S10–S16 (2006).
11. P. Cabrales, A. G. Tsai, and M. Intaglietta, "Is resuscitation from hemorrhagic shock limited by blood oxygen-carrying capacity or blood viscosity?" *Shock Waves* **27**, 380–389 (2007).
12. L. N. Torres, I. P. Torres Filho, R. W. Barbee, M. H. Tiba, K. R. Ward, and R. N. Pittman, "Systemic responses to prolonged hemorrhagic hypotension," *Am. J. Physiol. Heart Circ. Physiol.* **286**, H1811–H1820 (2004).
13. F. Gottrup, "Oxygen in wound healing and infection," *World J. Surg.* **28**, 312–315 (2004).
14. P. Melis, M. L. Noorlander, A. J. van der Kleij, C. J. van Noorden, and C. M. van der Horst, "Oxygenation and microcirculation during skin stretching in undermined and nonundermined skin," *Plast. Reconstr. Surg.* **112**, 1295–1301 (2003).
15. M. W. Dewhirst, "Concepts of oxygen transport at the microcirculatory level," *Semin. Radiat. Oncol.* **8**, 143–150 (1998).
16. R. K. Jain, "Determinants of tumor blood flow: a review," *Cancer Res.* **48**, 2641–2658 (1988).
17. P. Vaupel and L. Harrison, "Tumor hypoxia: causative factors, compensatory mechanisms, and cellular response," *Oncologist* **9** (Suppl. 5), 4–9 (2004).
18. T. A. Woolsey, C. M. Rovainen, S. B. Cox, M. H. Henegar, G. E. Liang, D. Liu, Y. E. Moskalenko, J. Sui, and L. Wei, "Neuronal units linked to microvascular modules in cerebral cortex: response elements for imaging the brain," *Cereb. Cortex* **6**, 647–660 (1996).
19. T. W. Secomb, R. Hsu, E. Y. H. Park, and M. W. Dewhirst, "Green's function methods for analysis of oxygen delivery to tissue by microvascular networks," *Ann. Biomed. Eng.* **32**, 1519–1529 (2004).
20. D. M. Brizel, B. Klitzman, J. M. Cook, J. Edwards, G. Rosner, and M. W. Dewhirst, "A comparison of tumor and normal tissue microvascular hematocrits and red cell fluxes in a rat window chamber model," *Int. J. Radiat. Oncol. Biol. Phys.* **25**, 269–276 (1993).
21. B. Klitzman and B. R. Duling, "Microvascular hematocrit and red cell flow in resting and contracting striated muscle," *Am. J. Physiol.* **237**, H481–H490 (1979).
22. A. K. Dunn, A. Devor, H. Bolay, M. L. Andermann, M. A. Moskowitz, A. M. Dale, and D. A. Boas, "Simultaneous imaging of total cerebral hemoglobin concentration, oxygenation, and blood flow during functional activation," *Opt. Lett.* **28**, 28–30 (2003).
23. R. D. Shonat, E. S. Wachman, W.-H. Niu, A. P. Koretsky, and D. L. Farkas, "Near-simultaneous hemoglobin saturation and oxygen tension maps in mouse brain using an AOTF microscope," *Biophys. J.* **73**, 1223–1231 (1997).
24. B. Styp-Rekowska, N. M. Disassa, B. Reglin, L. Ulm, H. Kuppe, T. W. Secomb, and A. R. Pries, "An imaging spectroscopy approach for measurement of oxygen saturation and hematocrit during intravital microscopy," *Microcirculation* **14**, 207–221 (2007).
25. B. S. Sorg, M. E. Hardee, N. Agarwal, B. J. Moeller, and M. W. Dewhirst, "Spectral imaging facilitates visualization and measurements of unstable and abnormal microvascular oxygen transport in tumors," *J. Biomed. Opt.* **13**, 014026 (2008).
26. B. S. Sorg, B. J. Moeller, O. Donovan, Y. Cao, and M. W. Dewhirst, "Hyperspectral imaging of hemoglobin saturation in tumor microvasculature and tumor hypoxia development," *J. Biomed. Opt.* **10**, 044004 (2005).
27. M. L. Ellsworth, R. N. Pittman, and C. G. Ellis, "Measurement of hemoglobin oxygen saturation in capillaries," *Am. J. Physiol.* **252**, H1031–H1040 (1987).
28. H. Kerger, G. Groth, K. Kalenka, P. Vajkoczy, A. G. Tsai, and M. Intaglietta, " pO_2 measurements by phosphorescence quenching: characteristics and applications of an automated system," *Microvasc. Res.* **65**, 32–38 (2003).
29. L. S. Ziemer, W. M. F. Lee, S. A. Vinogradov, C. Sehgal, and D. F. Wilson, "Oxygen distribution in murine tumors: characterization using oxygen-dependent quenching of phosphorescence," *J. Appl. Physiol.* **98**, 1503–1510 (2005).
30. D. Fukumura, L. Xu, Y. Chen, T. Gohongi, B. Seed, and R. K. Jain, "Hypoxia and acidosis independently up-regulate vascular endothelial growth factor transcription in brain tumors *in vivo*," *Cancer Res.* **61**, 6020–6024 (2001).
31. A. S. Golub and R. N. Pittman, "Erythrocyte-associated transients in PO_2 revealed in capillaries of rat mesentery," *Am. J. Physiol. Heart Circ. Physiol.* **288**, H2735–H2743 (2005).
32. D. P. Swain and R. N. Pittman, "Oxygen exchange in the microcirculation of hamster retractor muscle," *Am. J. Physiol. Heart Circ. Physiol.* **256**, H247–H255 (1989).
33. J. L. Unthank, J. M. Lash, J. C. Nixon, R. A. Sidner, and H. G. Bohlen, "Evaluation of carbocyanine-labeled erythrocytes for microvascular measurements," *Microvasc. Res.* **45**, 193–210 (1993).
34. D. Feng, D. Marshburn, F. Jen, R. J. Weinberg, R. M. Taylor II, and A. Burette, "Stepping into the third dimension," *J. Neurosci.* **27**, 12757–12760 (2007).
35. M. T. Fallon, "Rats and mice," in *Handbook of Rodent and Rabbit Medicine*, K. Laber-Laird, M. M. Swindle, and P. Flecknell, eds. (Elsevier Science, 1996), pp. 1–38.
36. R. D. Braun, J. L. Lanzen, and M. W. Dewhirst, "Fourier analysis of fluctuations of oxygen tension and blood flow in R3230Ac tumors and muscle in rats," *Am. J. Physiol.* **277**, H551–H568 (1999).
37. L. I. Cardenas-Navia, D. Yu, R. D. Braun, D. M. Brizel, T. W. Secomb, and M. W. Dewhirst, "Tumor-dependent kinetics of partial pressure of oxygen fluctuations during air and oxygen breathing," *Cancer Res.* **64**, 6010–6017 (2004).
38. J. Lanzen, R. D. Braun, B. Klitzman, D. Brizel, T. W. Secomb, and M. W. Dewhirst, "Direct demonstration of instabilities in oxygen concentrations within the extravascular compartment of an experimental tumor," *Cancer Res.* **66**, 2219–2223 (2006).
39. K. G. Brurberg, H. K. Skogmo, B. A. Graff, D. R. Olsen, and E. K. Rofstad, "Fluctuations in pO_2 in poorly and well-oxygenated spontaneous canine tumors before and during fractionated radiation therapy," *Radiother. Oncol.* **77**, 220–226 (2005).
40. K. G. Brurberg, M. Thuen, E.-B. M. Ruud, and E. K. Rofstad, "Fluctuations in pO_2 in irradiated human melanoma xenografts," *Radiat. Res.* **165**, 16–25 (2006).
41. A. Vadapalli, R. N. Pittman, and A. S. Popel, "Estimating oxygen transport resistance of the microvascular wall," *Am. J. Physiol. Heart Circ. Physiol.* **279**, 657–671 (2000).
42. W. G. Hundley, G. J. Renaldo, J. E. Levasseur, and H. A. Kontos, "Vasomotion in cerebral microcirculation of awake rabbits," *Am. J. Physiol.* **254**, H67–H71 (1988).
43. C. E. Riva, C. J. Pournaras, C. L. Poiry-Yamate, and B. L. Petrig, "Rhythmic changes in velocity, volume, and flow

- of blood in the optic nerve head tissue," *Microvasc. Res.* **40**, 36–45 (1990).
44. S. Bertuglia, A. Colantuoni, G. Coppini, and M. Intaglieta, "Hypoxia- or hyperoxia-induced changes in arteriolar vasomotion in skeletal muscle microcirculation," *Am. J. Physiol.* **260**, H362–H372 (1991).
 45. H. Kimura, R. D. Braun, E. T. Ong, R. Hsu, T. W. Secomb, D. Papahadjopoulos, K. Hong, and M. W. Dewhirst, "Fluctuations in red cell flux in tumor microvessels can lead to transient hypoxia and reoxygenation in tumor parenchyma," *Cancer Res.* **56**, 5522–5528 (1996).
 46. J. L. Lanzen, R. D. Braun, A. L. Ong, and M. W. Dewhirst, "Variability in blood flow and pO_2 in tumors in response to carbogen breathing," *Int. J. Radiat. Oncol. Biol. Phys.* **42**, 855–859 (1998).
 47. M. W. Dewhirst, Y. Cao, and B. J. Moeller, "Cycling hypoxia and free radicals regulate angiogenesis and radiotherapy response," *Nat. Rev. Cancer* **8**, 425–437 (2008).
 48. E. M. Lord, L. Harwell, and C. J. Koch, "Detection of hypoxic cells by monoclonal antibody recognizing 2-nitroimidazole adducts," *Cancer Res.* **53**, 5721–5726 (1993).
 49. M. C. Skala, K. M. Riching, A. Gendron-Fitzpatrick, J. Eickhoff, K. W. Eliceiri, J. G. White, and N. Ramanujam, "*In vivo* multiphoton microscopy of NADH and FAD redox states, fluorescence lifetimes, and cellular morphology in precancerous epithelia," *Proc. Natl. Acad. Sci. USA* **104**, 19494–19499 (2007).
 50. R. K. Jain, "Normalization of tumor microvasculature: an emerging concept in antiangiogenic therapy," *Science* **307**, 58–62 (2005).
 51. F. Adhami, G. Liao, Y. M. Morozov, A. Schloemer, V. J. Schmithorst, J. N. Lorenz, R. S. Dunn, C. V. Vorhees, M. Wills-Karp, J. L. Degen, R. J. Davis, N. Mizushima, P. Rakic, B. J. Dardzinski, S. K. Holland, F. R. Sharp, and C.-Y. Kuan, "Cerebral ischemia-hypoxia induces intravascular coagulation and autophagy," *Am. J. Pathol.* **169**, 566–583 (2006).
 52. R. F. Gariano and T. W. Gardner, "Retinal angiogenesis in development and disease," *Nature* **438**, 960–966 (2005).
 53. M. W. Dewhirst, "Angiogenesis and blood flow in solid tumors," in *Drug Resistance in Oncology*, B. A. Teicher, ed. (Marcel Dekker, 1993), pp. 3–23.
 54. A. D. Estrada, A. Ponticorvo, T. N. Ford, and A. K. Dunn, "Microvascular oxygen quantification using two-photon microscopy," *Opt. Lett.* **33**, 1038–1040 (2008).
 55. C. B. Schaffer, B. Friedman, N. Nishimura, L. F. Schroeder, P. S. Tsai, F. F. Ebner, P. D. Lyden, and D. Kleinfeld, "Two-photon imaging of cortical surface microvessels reveals a robust redistribution in blood flow after vascular occlusion," *PLoS Biol.* **4**(2), e22 (2006).
 56. E. B. Brown, R. B. Campbell, Y. Tsuzuki, L. Xu, P. Carmeliet, D. Fukumura, and R. K. Jain, "*In vivo* measurement of gene expression, angiogenesis and physiological function in tumors using multiphoton laser scanning microscopy," *Nat. Med.* **7**, 864–868 (2001).
 57. D. Fu, T. Ye, T. E. Matthews, B. J. Chen, G. Yurtserver, and W. S. Warren, "High-resolution *in vivo* imaging of blood vessels without labeling," *Opt. Lett.* **32**, 2641–2643 (2007).
 58. K. Tsukada, E. Sekizuka, C. Oshio, K. Tsujioka, and H. Minamitani, "Red blood cell velocity and oxygen tension measurement in cerebral microvessels by double-wavelength photoexcitation," *J. Appl. Physiol.* **96**, 1561–1568 (2004).
 59. P. Vaupel, "Tumor microenvironmental physiology and its implications for radiation oncology," *Semin. Radiat. Oncol.* **14**, 198–206 (2004).
 60. J. D. Briers, "Laser Doppler, speckle and related techniques for blood perfusion mapping and imaging," *Physiol. Meas.* **22**, R35–R66 (2001).
 61. V. Rajan, B. Varghese, T. G. van Leeuwen, and W. Steenbergen, "Review of methodological developments in laser Doppler flowmetry," *Lasers Med. Sci.* (31 Jan. 2008).
 62. C. Hitzemberger, P. Trost, P.-W. Lo, and Q. Zhou, "Three-dimensional imaging of the human retina by high-speed optical coherence tomography," *Opt. Express* **11**, 2753–2761 (2003).
 63. J. A. Izatt, M. D. Kulkarni, S. Yazdanfar, J. K. Barton, and A. J. Welch, "*In vivo* bidirectional color Doppler flow imaging of picoliter blood volumes using optical coherence tomography," *Opt. Lett.* **22**, 1439–1441 (1997).
 64. R. Michaely, A. H. Bachmann, M. L. Villiger, C. Blatter, T. Lasser, and R. A. Leitgeb, "Vectorial reconstruction of retinal blood flow in three dimensions measured with high resolution resonant Doppler Fourier domain optical coherence tomography," *J. Biomed. Opt.* **12**, 041213 (2007).
 65. Y. Wang, B. A. Bower, J. A. Izatt, O. Tan, and D. Huang, "*In vivo* total retinal blood flow measurement by Fourier domain Doppler optical coherence tomography," *J. Biomed. Opt.* **12**, 041215 (2007).
 66. L. Kagemann, G. Wollstein, M. Wojtkowski, H. Ishikawa, K. A. Townsend, M. L. Gabriele, V. J. Srinivasan, J. G. Fujimoto, and J. S. Schuman, "Spectral oximetry assessed with high-speed ultra-high resolution optical coherence tomography," *J. Biomed. Opt.* **12**, 041212 (2007).
 67. C.-W. Lu, C.-K. Lee, M.-T. Tsai, Y.-M. Wang, and C. C. Yang, "Measurement of the hemoglobin oxygen saturation level with spectroscopic spectral-domain optical coherence tomography," *Opt. Lett.* **33**, 416–418 (2008).
 68. N. V. Iftimia, D. X. Hammer, C. E. Bigelow, D. I. Rosen, T. Ustun, A. A. Ferrante, D. Vu, and R. D. Ferguson, "Toward noninvasive measurement of blood hematocrit using spectral domain low coherence interferometry and retinal tracking," *Opt. Express* **14**, 3377–3388 (2006).